10568 *Macromolecules* **2010**, *43*, 10568–10581
DOI: 10.1021/ma101276d

Macromolecules
ARTICLE

Hierarchical Structure in Nanoscale Thin Films of a Poly(styrene-*b*-methacrylate grafted with POSS) (PS_{214}-*b*-$PMAPOSS_{27}$)

Byungcheol Ahn,[‡,†] Tomoyasu Hirai,[§,†] Sangwoo Jin,[‡,†] Yecheol Rho,[‡] Kwang-Woo Kim,[‡] Masa-aki Kakimoto,[§] Padma Gopalan,[⊥] Teruaki Hayakawa,*[,§] and Moonhor Ree*[,‡]

[‡]*Department of Chemistry, Pohang Accelerator Laboratory, Division of Advanced Materials Science, Center for Electro-Photo Behaviors in Advanced Molecular Systems, BK School of Molecular Science, and Polymer Research Institute, Pohang University of Science and Technology, Pohang 790-784, Republic of Korea,* [§]*Department of Organic and Polymeric Materials, Tokyo Institute of Technology, 2-12-1-S8-36 O-okayama, Meguro-ku Tokyo 152-8552, Japan, and* [⊥]*Department of Materials Science and Engineering, University of Wisconsin-Madison, Madison, Wisconsin 5376, United States.* [†]*These authors equally contributed to this study*

Received June 8, 2010; Revised Manuscript Received November 23, 2010

ABSTRACT: An interesting organic−inorganic diblock copolymer, poly(styrene-*b*-methacrylate grafted with polyhedral oligomeric silsesquioxane) (PS-*b*-PMAPOSS), with PS (an average degree of polymerization $\overline{DP}$ of 214) and PMAPOSS ($\overline{DP}$ = 27) blocks was prepared: PS_{214}-*b*-$PMAPOSS_{27}$. The morphological structures in nanoscale thin films of PS_{214}-*b*-$PMAPOSS_{27}$ and their temperature-dependent changes were investigated in detail by performing grazing incidence X-ray scattering (GIXS) with a synchrotron radiation source. GIXS formulas based on structural models were derived for the quantitative analysis of the two-dimensional (2D) scattering data. In addition, the thermal properties of the diblock copolymer were characterized: it was found to be stable up to 330 °C, and to undergo a glass transition at 96 °C (PS block) and a melting transition at 173 °C (PMAPOSS block). The quantitative 2D GIXS analysis found that the diblock copolymer molecules in the thin films undergo phase separation into PS and PMAPOSS domains, which generates a lamellar structure. Surprisingly, in the solvent-annealed films with and without subsequent thermal annealing the lamellar structure is completely oriented in the out-of-plane of the film and is stable up to the degradation temperature. The PMAPOSS layers in the lamellar structure were found to consist of two sublayers, namely a densely ordered layer composed of vertically oriented orthorhombic crystals and a less ordered layer that consists of molecularly stacked layers that are oriented vertically. In both the sublayers, the PMAPOSS block chains have helical conformations and thus are present as molecular cylinders. These molecular cylinders are always oriented in the film plane. On heating, the orthorhombic crystals and the molecularly stacked layers melt over the range 170−190 °C. On subsequent cooling, the orthorhombic crystals and molecularly stacked layers are not fully recovered, which indicates that the formation of orthorhombic crystals and stacked layers in the PMAPOSS domains requires thermal annealing.

Introduction

The sizes of the self-assembled nanostructures that form in thin films of block copolymers can be tuned from a few nanometers to hundreds of nanometers by varying their chemical composition and molecular weight.[1−6] Thus, much research effort has been applied to the fabrication of well-ordered morphologies, to improving functionality by modifying chemical components, and even to the preparation of block copolymers with both well-ordered morphology and enhanced functionality.[1−6]

In particular, the interest in inorganic−organic hybrid block copolymers has increased because the presence of inorganic materials in block copolymers results in properties that cannot be achieved in organic−organic block copolymers.[7−13] In general, inorganic materials are immiscible with organic polymers, which results in large scale phase separation.[7−13] Therefore, attempts have been made to directly bridge between the inorganic material components and the block copolymers via covalent bond formation in order to prevent self-aggregation of the inorganic components and to minimize large scale phase separation.[7−13] Several inorganic materials such as metallocene and polyhedral oligomeric silsesquioxane (POSS) units have been used in the inorganic−organic hybridization of block copolymers.[8−13]

Block copolymers containing POSS units are particularly interesting because they exhibit good thermal and mechanical properties, as well as high resistance to oxidation.[10−13] It is also a merit of incorporated POSS units that they can be converted to silica by exposure to oxygen plasma.[10−13] Recently, we reported a series of novel inorganic−organic block copolymers composed of polymethacrylate grafted with POSS and either polystyrene or poly(methyl methacrylate), which were synthesized by using living anionic polymerization and exhibit phase-separated morphology in the bulk state.[14] However, the structural details of these diblock copolymer systems have not previously been investigated, even in the bulk state. Quantitative structural analysis is thus necessary to determine the properties and applications of these interesting inorganic−organic hybrid diblock copolymers.

In this study, we synthesized a diblock copolymer composed of a polystyrene (PS) block with an average degree of polymerization $\overline{DP}$ of 214 and a polymethacrylate grafted with POSS (PMAPOSS) block with $\overline{DP}$ = 27 (PS_{214}-*b*-$PMAPOSS_{27}$) (Figure 1) by using living anionic polymerization, and investigated its structure and orientation details in nanoscale thin films by using grazing incidence X-ray scattering (GIXS) with a synchrotron radiation source. In addition, the temperature-dependent structural changes in the

*To whom correspondence should be addressed. E-mail: ree@postech.edu (M.R.); hayakawa.t.ac@m.titech.ac.jp (T.H.). Telephone: +82-54-279-2120 (M.R.), +81-3-5734-2421 (T.H.).

 Published on Web 12/06/2010

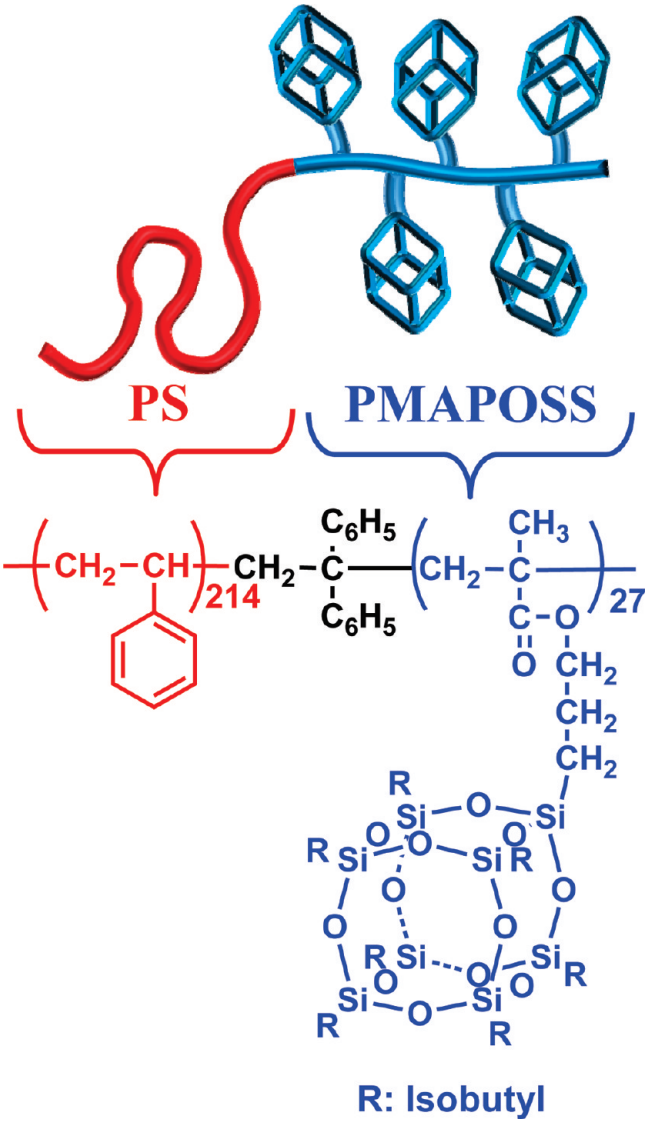

Figure 1. Chemical structure of the organic−inorganic diblock copolymer (PS_{214}-*b*-$PMAPOSS_{27}$) composed of a linear polystyrene (PS) block and a brush polymethacrylate block bearing polyhedral oligomeric silsesquioxane at the bristle end (PMAPOSS).

thin films were studied in situ during heating and subsequent cooling.

Experimental Section

Materials and Thin Film Preparation. An inorganic−organic diblock copolymer, PS_{214}-*b*-$PMAPOSS_{27}$ was synthesized by living anionic polymerization method as reported previously in the literature.[14] In addition, a PMAPOSS homopolymer was prepared. The $\overline{DP}$ values of the block components were determined by the integrated intensities of proton nuclear magnetic resonance spectroscopy. The overall number-average molecular weight $\overline{M}_n$ and $\overline{DP}$ of the diblock copolymer were determined to be 47 500 and 1.09, respectively, by gel permeation chromatography (GPC). The GPC analysis was extended to the hompolymer and found that its $\overline{M}_n$ and $\overline{DP}$ are 57 200 and 1.07 respectively.

The diblock copolymer was dissolved in cyclopentanone and filtered using a disposable syringe equipped with a polytetrafluoroethylene filter of pore size 0.2 μm, producing a solution of 2 wt % polymer. This filtered solution was spin-coated onto precleaned silicon substrates and dried at room temperature under vacuum for 24 h. Then, the obtained films were treated either by solvent-annealing at room temperature under carbon disulfide (CS_2) vapor for 36 h, followed by drying at room temperature under vacuum for 36 h or by thermal annealing at 170 °C for 12 h under vacuum. Some of the solvent-annealed films were further thermally annealed at 170 °C for 12 h under vacuum. The prepared diblock copolymer films were determined to have a thickness of 70−80 nm by using a spectroscopic ellipsometer (model M2000, J. A. Woollam, Lincoln, NE).

Measurements. GIXS measurements were accomplished at the 4C2 beamline[15−18] at the Pohang Accelerator Laboratory.[19] The samples were measured at a sample-to-detector distance (SDD) of 2170 mm for grazing incidence small-angle X-ray scattering (GISAXS), and 129 mm for grazing incidence wide-angle X-ray scattering (GIWAXS). The GIXS measurements were carried out on the film samples during heating over the temperature range 25−320 °C and subsequent cooling; a rate of 2.0 °C/min was employed for the heating and cooling runs. Scattering data were typically collected for 20 or 30 s using an X-ray radiation source (a size of 0.5 mm height × 0.8 mm width) of $\lambda = 0.138$ nm with a two-dimensional (2D) charge-coupled detector (CCD) (model PI-SCX4800, Roper Scientific, Trenton, NJ) (Figure 2). The incidence angle α_i of each X-ray beam was set in the range 0.140−0.200°, which is between the critical angles of the diblock copolymer film and the silicon substrate ($\alpha_{c,f}$ and $\alpha_{c,s}$). Scattering angles were corrected according to the positions of the X-ray beams reflected from the silicon substrate with respect to a precalibrated silver behenate (TCI, Japan) powder. Aluminum foil pieces were applied as a semitransparent beam stop, because the intensity of the specular reflection from the substrate is much stronger than the intensity of GIXS near the critical angle.

Atomic force microscopy (AFM) measurements were performed to observe topography images of the diblock copolymer thin films. The spin-coated PS-*b*-PMAPOSS films were imaged using a scanning probe microscope (model Multimode Nanoscope IIIa, Veeco, Santa Clara, CA) in tapping mode, which was equipped with a JV-scanner; noncoated silicon etched probes (model LTESP, Veeco) were used in the measurements. Thermogravimetric analysis (TGA) and differential scanning calorimetry (DSC) measurements were carried out under a nitrogen atmosphere using a thermogravimeter (model TG/DTA 6200, Seiko Instruments, Japan) and a calorimeter (model DSC 6200, Seiko Instruments, Japan). A rate of 5.0 °C/min was employed for heating and cooling runs.

Results and Discussion

The thermal properties of the PS_{214}-*b*-$PMAPOSS_{27}$ polymer were investigated under a nitrogen atmosphere. The diblock copolymer was found to start thermal degradation at 330 °C ($= T_d$) (Figure 3A). Phase behaviors of the diblock copolymer were examined over the temperature range 0−250 °C by DSC analysis. The DSC analysis was extended for its PMAPOSS homopolymer. The obtained DSC thermograms are shown in Figure 3B.

On heating, the PMAPOSS homopolymer reveals two endothermic transitions and one exothermic transition (Figure 3B). The first endothermic peak appears around 43 °C, which is weak and broad, showing typical characteristic of glass transition. Thus, this peak can be assigned as glass transition of the homopolymer. This glass transition temperature (T_g) is much lower than that (around 100 °C) of poly(methyl methacrylate) (PMMA) which has same backbone. Considering the bulky, massive POSS pendant, the homopolymer is expected to have higher T_g than that of PMMA. However, the expectation is in contrast to the observation. Thus, the observed low T_g might be attributed to role of seven flexible isobutyl groups per POSS pendant which can mobilize the POSS pendant. One exothermic peak is observed around 159 °C. POSS molecules are known to crystallize.[11] Taking this fact into account, the observed exothermic peak originates from cold crystallization of the homopolymer which takes place during the heating run. From this result, the second

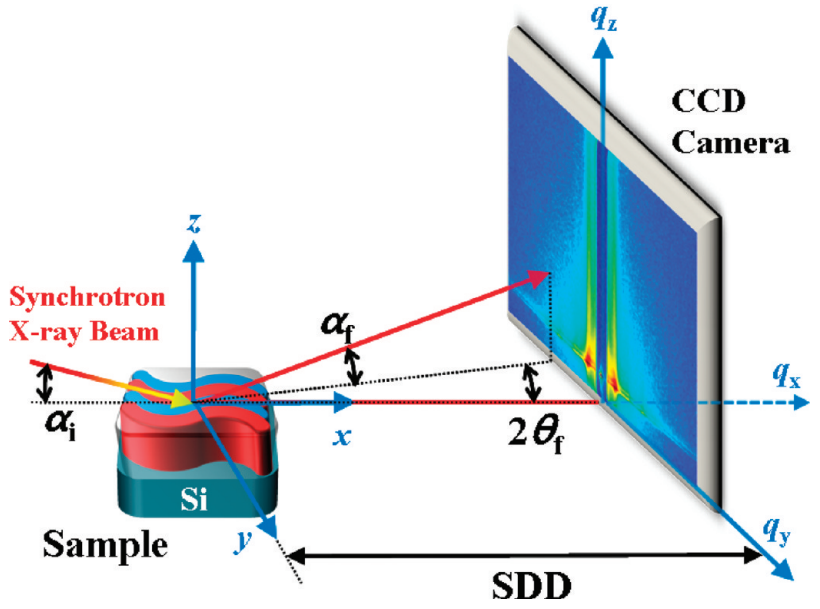

Figure 2. Geometry of GIXS: α_i is the incident angle at which the X-ray beam impinges on the film surface; α_f and $2\theta_f$ are the exit angles of the X-ray beam with respect to the film surface and to the plane of incidence respectively, and q_x, q_y, and q_z are the components of the scattering vector **q**.

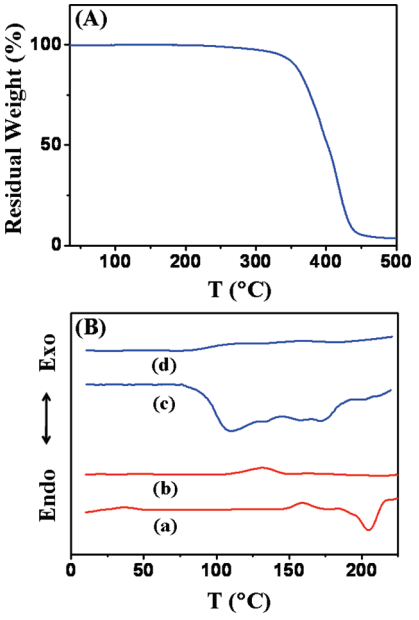

Figure 3. (A) TGA thermogram of the PS_{214}-*b*-$PMAPOSS_{27}$ polymer. (B) DSC thermograms of the PS_{214}-*b*-$PMAPOSS_{27}$ polymer and PMAPOSS homopolymer: (a and b) heating and subsequent cooling runs of the homopolymer respectively; (c and d) heating and subsequent cooling runs of the diblock copolymer, respectively. The TGA and DSC measurements were carried out at a rate of 5.0 °C/min under nitrogen atmosphere.

endothermic peak around 205 °C can be assigned as melting of the homopolymer crystals. On cooling run from the melt, crystallization exothermic peak is discernible around 132 °C but glass transition apparently is not observable.

With the phase behaviors observed for the homopolymer, we attempted to analyze the DSC thermograms measured for the diblock copolymer. As can be seen in Figure 3B, the diblock copolymer reveals only two endotherms on heating run although having two blocks with different chemical compositions. The first transition appears clearly around 96 °C. This transition shows typical nature of glass transition and its temperature is close to the glass transition temperature (T_g) of conventional polystyrene. Considering these facts, this transition can be assigned as glass transition of the PS block. Moreover, the observation of the PS block' glass transition indicates that the PS block is phase-separated from the PMAPOSS block, forming its own phase domains. The second endothermic peak appears around 173 °C. The POSS pendant units in copolymers of ethylene and POSS-containing macromonomer were reported to have tendency to aggregate and crystallize as nanocrystals.[12,20] Taking into account this fact as well as the DSC results of PMAPOSS homopolymer discussed above, the second endothermic peak originates from melting of the crystals formed in phase-separated domains of the PMAPOSS block. This melting point is relatively lower than that observed for the PMAPOSS homopolymer. The low melting point in the diblock copolymer might be attributed to the relatively low molecular weight of the PMAPOSS block, compared to that of the homopolymer. Beyond these two endothermic peaks, glass transition of the PMAPOSS block is expected to appear around 43 °C (= T_g (homopolymer)). Further, exothermic peak due to possible cold crystallization of the PMAPOSS block is expected to appear because such cold crystallization behavior was detected for the homopolymer as discussed above. However, they could not be discernible in the heating run (Figure 3B). No observation of these peaks in the heating run might be due to several possible factors as follows. First, PMAPOSS shows intrinsically very weak glass transition behavior, which was confirmed even for the high molecular weight hompolymer as discussed above. Second, the PMAPOSS block is the minor component in the diblock copolymer and further has relatively low molecular weight. Finally, crystallization of the PMAPOSS block could not be detectable even in cooling run from melt (Figure 3B). Thus, in heating run it may be very hard to detect cold crystallization of the PMAPOSS block.

With the above thermal analysis results, GIXS measurements were carried out on thin films of PS_{214}-*b*-$PMAPOSS_{27}$ to investigate any possible phase-separated domain structure between the PS and PMAPOSS blocks and molecular packing structure in the individual domains, simultaneously.

Figure 4a shows the representative 2D GISAXS pattern obtained at $\alpha_i = 0.147°$ for the diblock copolymer films prepared by solvent-annealing under CS_2 vapor and subsequently thermal annealing at 170 °C. Similar scattering patterns were observed over the α_i range of 0.14−0.20°, which are between $\alpha_{c,f}$ and $\alpha_{c,s}$

(data not shown). In Figure 4a, the X-ray beam reflected from the Si substrate is observed at $2\theta_f = 0°$, which was attenuated by semitransparent beam stop. And a series of scattering peaks are observed along the $2\theta_f$ direction. They are placed periodically and symmetrically from the reflected X-ray beam. And also highly intense scattering strips are overlapped on those scattering peaks along the $2\theta_f$ direction, whose exit angles (α_f) cover a range between the critical angle of the film and silicon substrate. Such the scattering strips originate from the combination of a type of standing wave phenomenon and total reflection at the interface between the film and the substrate, as often observed in the scattering patterns from other polymer thin films.[16,21]

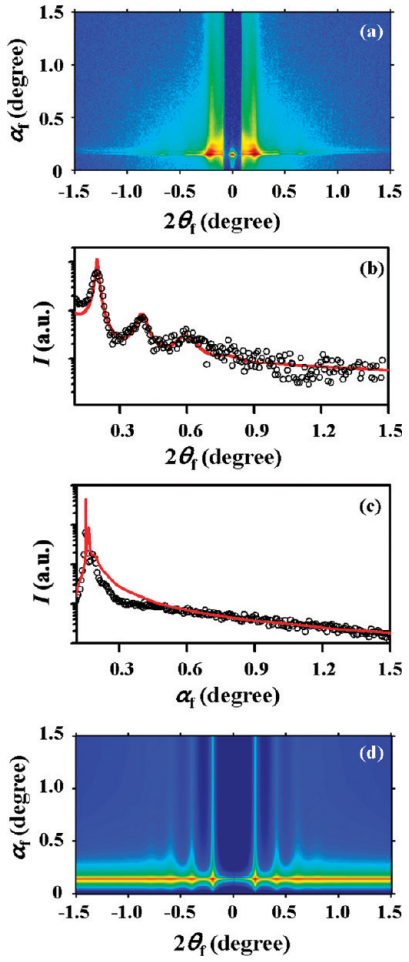

Figure 4. (a) 2D GISAXS pattern measured at 25 °C with $\alpha_i = 0.147°$ for a 70 nm thick PS_{214}-*b*-$PMAPOSS_{27}$ film deposited on a silicon substrate. Here the film was prepared by solvent-annealing under CS_2 vapor and subsequently thermal annealing at 170 °C. (b) In-plane scattering profile extracted from the GISAXS pattern in part a along the $2\theta_f$ direction at $\alpha_f = 0.170°$. (c) Out-of-plane scattering profile extracted from the GISAXS pattern in part a along the α_f direction at $2\theta_f = 0.200°$. In parts b and c, the symbols are the measured data and the red lines are obtained by fitting the measured data using the GIXS formula. (d) 2D GISAXS pattern reconstructed for the PS_{214}-*b*-$PMAPOSS_{27}$ films by using the GIXS formula with the structural parameters in Table 1.

To obtain further structural information from the GISAXS pattern, we acquired the in-plane and out-of-plane scattering profiles. Parts b and c of Figure 4 show the in-plane and out-plane scattering profiles, which were extracted from the 2D GISAXS (Figure 4a) along the $2\theta_f$ direction at $\alpha_f = 0.170°$ and along the α_f direction at $2\theta_f = 0.200°$, respectively. As can be seen in Figure 4b, the in-plane scattering profile shows periodic scattering peaks at relative $2\theta_f$ positions from the specular reflection position of 1, 2, 3, and 4; their scattering vector lengths are 0.160, 0.321, 0.498, and 0.647 nm^{-1} respectively. This scattering feature is indicative of lamellar stacks formed in the film. On the other hand, the out-of-plane scattering profile shows peaks in the low angle region of $\alpha_f < 0.3°$, which are attributed to the standing wave phenomenon and total reflection (see Figure 4a) but featureless at $\alpha_f > 0.3°$. In particular, the featureless scattering profile at $\alpha_f > 0.3°$ decays with the square of scattering vector, which is a characteristic feature of disk-type scatterer. These in-plane and out-of-plane scattering results collectively inform that in the film, a lamellar structure is formed where the individual lamellar layers are oriented in the out-of-plane of the film. The long period of such the vertically oriented lamellar stacks is estimated to be 39.2 nm from the periodic scattering peaks along the $2\theta_f$ direction. From these results, a structural model for the lamellar stacks formed in the films is proposed as shown in Figure 5a.

To obtain structural details about the lamellar structure formed in the diblock copolymer films, we have attempted to quantitatively analyze the measured 2D GISAXS pattern by using the GIXS formula derived in Appendix 1 for the multilayer structures in thin films. As shown in parts b and c of Figure 4, the in-plane and out-of-plane scattering profiles (which were extracted along the $2\theta_f$ direction at $\alpha_f = 0.170°$ and along the α_f direction at $2\theta_f = 0.200°$, respectively) can be satisfactorily fitted with this GIXS formula, which confirms that the measured GISAXS pattern was successfully analyzed. From this quantitative analysis, the structural parameters of the lamellar structure formed in the diblock copolymer thin film were obtained. The results are summarized in Table 1.

The quantitative GISAXS analysis found that the lamellar structure in the film is composed of three layers: (i) an amorphous PS layer, (ii) an ordered (i.e., dense) PMAPOSS layer in which the POSS units are stacked regularly, and (iii) a less ordered PMAPOSS layer that acts an interface between the amorphous PS layer and the ordered PMAPOSS layer (Figure 5b). Surprisingly, the individual layers are perfectly oriented normal to the film plane and are stacked together parallel to the film plane

Furthermore, from the structural parameters acquired above, the 2D GISAXS pattern was reconstructed by using the GIXS formula. The reconstructed 2D GISAXS pattern is displayed in Figure 4d. The reconstructed 2D GISAXS pattern is in good agreement with the measured 2D GISAXS pattern in Figure 4a.

In addition to the GISAXS analysis, the surface of the diblock copolymer film was examined with AFM analysis in order to

Table 1. Microstructural Parameters of Thin Films of PS_{214}-*b*-$PMAPOSS_{27}$ at Various Temperatures, Which Were Obtained by GISAXS Measurements and Data Analyses

T (°C)	d_{x1}[a] (nm)	d_{x2}[b] (nm)	d_{x3}[c] (nm)	σ_{x1}[d] (nm)	σ_{x2}[d] (nm)	σ_{x3}[d] (nm)	g_1[e]	φ[f] (deg)
25	2.9	13.0	20.4	0.4	1.0	1.2	0.098	0
150	4.5	8.0	22.2	0.5	0.9	2.1	0.164	0
200	7.6	2.2	21.8	0.5	0.8	2.4	0.176	0
30	2.6	12.4	21.6	0.4	1.2	1.5	0.118	0

[a] Thickness of less ordered PMAPOSS layer. [b] Thickness of densely ordered PMAPOSS layer. [c] Thickness of amorphous PS layer. [d] Standard deviation of layer thickness. [e] Paracrystal distortion factor along the direction parallel to the long period of lamellar structure, which is defined by $\Delta\mathbf{a}_1/\mathbf{a}_1$ where $\mathbf{a}_1$ is a component of the fundamental vector $\mathbf{a}$ of the lamellar structure and $\Delta\mathbf{a}_1$ is the displacement of $\mathbf{a}_1$. [f] Orientation of the lamellar structure with respect to the direction normal to the film plane.

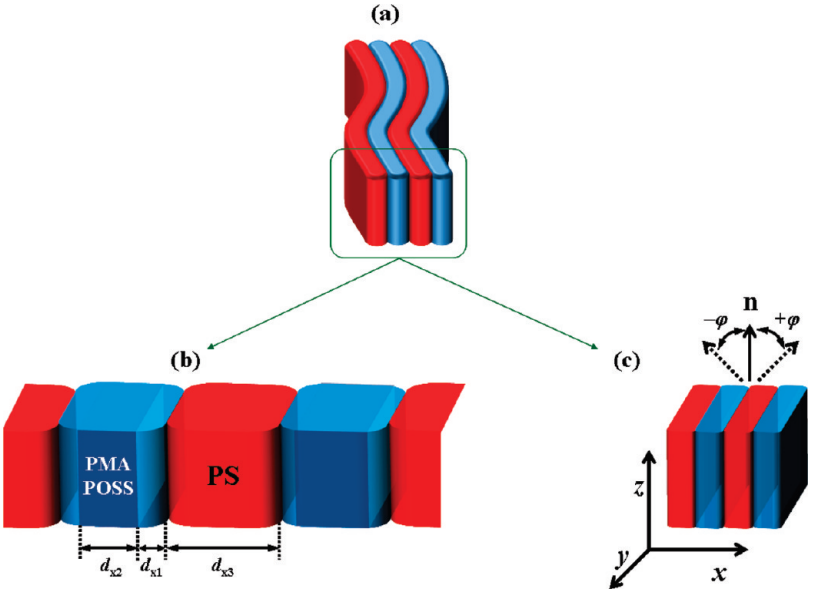

Figure 5. (a) Schematic representation of the lamellar structure of the PS_{214}-*b*-$PMAPOSS_{27}$ polymer consisting of phase-separated PS and PMAPOSS layer domains in a thin film that was thermally annealed. (b) The individual PMAPOSS layers are composed of two sublayers, namely a densely ordered layer and a less ordered layer: d_{x1}, d_{x2}, and d_{x3} are the thicknesses of the less ordered PMAPOSS layer, the densely ordered PMAPOSS layer, and the amorphous PS layer, respectively. (c) Orientation of the lamellar structure: **n** is the vector of the lamellar orientation axis, which is normal to the long period between lamellae, and φ is the polar angle between the **n** vector and the out-of-plane direction of the film.

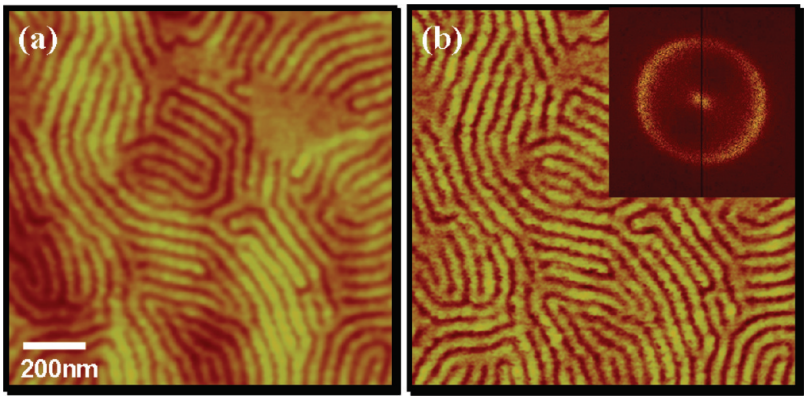

Figure 6. Representative AFM (a) height image and (b) phase image (1000 × 1000 nm^2) of PS_{214}-*b*-$PMAPOSS_{27}$ films (70 nm thick) deposited on silicon substrates. The inset shows the Fourier transform of the AFM phase image.

further visualize the lamellar structure formed in the film. Figure 6 shows a representative AFM height and phase image of a film obtained at 25 °C. The distinctive feature of the AFM image is the fingerprint pattern of the lamellar structure formed in the film. From the Fourier transform of the AFM phase image shown at inset of Figure 6b, the interdistance between the PS (or PMAPOSS) domains was estimated to be 41.6 nm. This interdistance is slightly larger than that (39.2 nm) determined from the GISAXS analysis. In addition, the film surface was estimated to have a root-mean-square roughness of 2.2 nm, which might be associated with the vertically oriented lamellar structure formed in the film as a result of the solvent and subsequent thermal annealing.

In addition, the diblock copolymer films, which were prepared either by only solvent-annealing or by only thermal annealing, were investigated by using GISAXS. The GISAXS analysis found that the solvent-annealed films show the formation of vertically oriented lamellar structure as observed in the films treated by solvent-annealing and subsequently thermal annealing while the thermally annealed films reveal the formation of randomly oriented lamellar structure (data not shown). In particular, the randomly oriented lamellar structure formed in the thermally annealed film is quite different from the vertically oriented lamellar structure observed in the solvent-annealed film. Moreover, the lamellar structure in the thermally annealed film was found to reveal relatively poor ordering in comparison to those of the films treated by solvent-annealing with and without subsequently thermal annealing. Regarding these results, for the PS_{214}-*b*-$PMAPOSS_{27}$ films onto the silicon substrates with native oxide layer, an appropriate solvent-annealing is necessary to make highly ordered lamellar structure composed of vertically oriented layers.

In case of the solvent-annealing in this study, the CS_2 solvent has better affinity to the PS block compared to the PMAPOSS block and, thus the solvent vapor preferentially mobilizes the PS blocks, promoting microstructure formation (namely, lamellar structure formation) based on phase-separation between the PS and PMAPOSS blocks during the solvent-annealing. Further, the solvent vapor promotes the phase-separated PS domains to properly balance out of their surface energy with that of the phase-separated PMAPOSS domains in regard to surface energy of the silicon substrate, inducing the stack formation of vertically oriented layers with respect to the film plane.

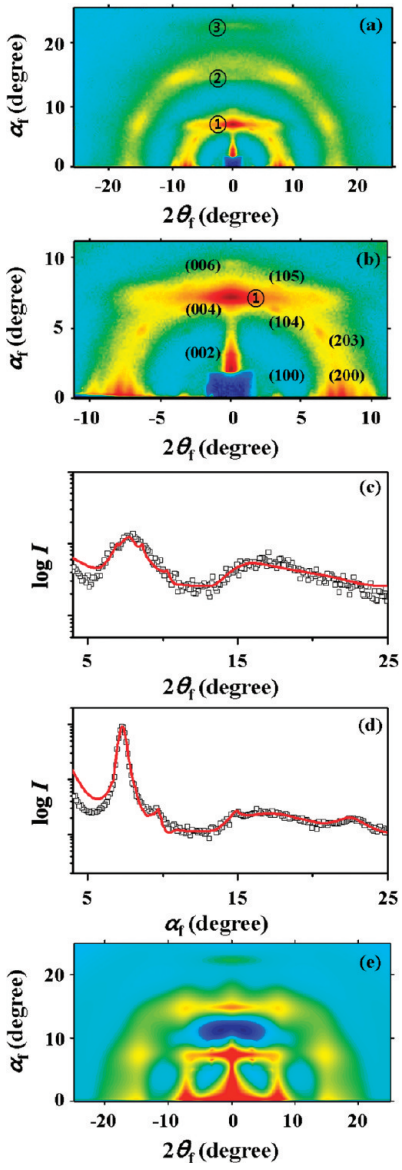

Figure 7. (a) 2D GIWAXS pattern measured at 25 °C with $\alpha_i = 0.150°$ for a 70 thick PS_{214}-*b*-$PMAPOSS_{27}$ film deposited on a silicon substrate; here the film was prepared by solvent-annealing under CS_2 vapor and subsequently thermal annealing at 170 °C. (b) Enlarged pattern of the 2D GIWAXS data in part a: scattering spots were indexed with orthorhombic lattice. (c) In-plane scattering profile extracted from the GIWAXS pattern in part a along the $2\theta_f$ direction at $\alpha_f = 0.30°$. (d) Out-of-plane scattering profile extracted from the GIWAXS pattern in part a along the α_f direction at $2\theta_f = 0.0°$; the black symbols are the measured data and the red solid lines were obtained by fitting the data using the GIXS formula. The GIXS analysis results are summarized in Table 2. (e) 2D GIWAXS pattern reconstructed by using the GIXS formula with the structural parameters in Table 2.

As discussed above, the DSC analysis found that on heating run the diblock copolymer sample reveals an endothermic peak relating to melting of crystals. Thus, GIWAXS measurements were performed to investigate any crystal formation at molecular scale in the diblock copolymer films, in addition to the GISAXS analysis. Figure 7a shows the representative 2D GIWAXS pattern obtained at $\alpha_i = 0.150°$ for the diblock copolymer films prepared by solvent-annealing under CS_2 vapor and subsequently thermal annealing at 170 °C. As can be seen in this figure, the 2D GIWAXS pattern is very complicated. This scattering pattern is apparently composed of three groups of diffractions. The first group consists of a series of diffraction peaks (marked with circled numbers in the figure), which are located at 7.35, 14.7, and 22.2° along the α_f direction at $2\theta_f = 0°$ (i.e., the out-of-plane of the film). It was found that peak 1 is the first-order diffraction and that peaks 2 and 3 are the second- and third-order diffractions of peak 1. The first- and second-order diffractions are observed along the $2\theta_f$ direction at $\alpha_f = 0°$ (i.e., the in-plane of the film). The *d*-spacing of the first-order diffraction peak was determined to be 1.08 nm. This *d*-spacing is identical to the molecular size of the POSS units estimated from the geometrical optimization of the molecules with the *Cerius*[2] software package (Accelrys, San Diego, CA). Thus, the *d*-spacing value can be assigned to the interdistance of the POSS units. These diffraction peaks indicate that the POSS units in the PMAPOSS domains are more likely to pack in a regular manner along the out-of-plane of the film as well as the in-plane of the film; thus the POSS units form a molecularly packed layer structure that is oriented along the out-of-plane and the in-plane of the film even though a well-defined lattice cannot be formed.

The second group of scattering peaks consists of two amorphous halo rings (Figure 7a). The amorphous halo peak near 17.8° was determined to have a *d*-spacing of 0.47 nm. This *d*-spacing value corresponds to the interdistance between the polymer chains and the side groups in the PS domains. Thus, the amorphous halo ring is attributed to the amorphous PS domains. The other amorphous halo centered at 7.35° was determined to have a *d*-spacing of 1.08 nm. This *d*-spacing value is the same as the size of the POSS units. Thus, this amorphous ring arises from the interdistance between the polymer chains and the POSS-containing side groups in the amorphous region of the PMAPOSS domains, which indicates that a fraction of the amorphous phase is present in the PMAPOSS domains. Note that this amorphous halo overlaps with the first-order diffraction peak of the POSS units in the molecularly packed layer structure, which results in the significant enhancement of the intensity of the first-order diffraction peak.

The third group of scattering peaks is a series of diffraction spots at regular intervals (Figure 7a). These diffraction spots overlap significantly with the two amorphous halo rings discussed above. In fact, the PMA backbone in the PMAPOSS block has amorphous characteristics. In contrast, as discussed above, the POSS units have a tendency to aggregate and crystallize as nanocrystals.[11,12,20] Thus, the observed diffraction spots originate from the well-defined lattice-like ordered structure of POSS units in the PMAPOSS domains. To further examine the observed scattering spots, a scattering area ($\alpha_f = 0-11°$, and $2\theta_f = -11$ to $+11°$) containing those scattering spots that overlap with the amorphous halo in the low angle region was selected and is enlarged in Figure 7b. As can be seen in this figure, a set of scattering spots appear along the amorphous halo near 7.35°. On the right-hand side of the scattering pattern, the two scattering spots due to the ordered PMAPOSS domains are positioned at azimuthal angles of 36 and 64° respectively with respect to the $2\theta_f$ direction at $\alpha_f = 0°$. The positions of these scattering spots differ slightly from the azimuthal angles of 30 and 60° respectively with respect to the $2\theta_f$ direction at $\alpha_f = 0°$ that are characteristic of a hexagonally packed structure. These slight mismatches suggest that the molecular order formed in the PMAPOSS domains is most likely orthorhombic rather than hexagonal. The scattering spots were successfully indexed by adopting an orthorhombic lattice (Figure 7b). From the indexed scattering spots, the lattice dimensions were estimated to be 4.87 nm along the out-of-plane of the film, and 2.47 and 1.16 nm in the film plane. In particular, the dimensional parameter, 1.16 nm in the film plane, was found to be very close to the length of the chemically repeating unit along the PMAPOSS block backbone in the helical conformation. Moreover, the orthorhombic lattice was found to be oriented along the out-of-plane of the film. These scattering results indicate

Table 2. Structural Parameters of Thin Films of PS_{214}-*b*-$PMAPOSS_{27}$, Which Were Obtained by GIWAXS Measurements and Data Analysis

d_y[a] (nm)	d_z[a] (nm)	$d_{PMAPOSS}$[b] (nm)	d_{PS}[c] (nm)	R[d] (nm)	g_y[e]	g_z[e]	$g_{h(PMAPOSS)}$[f]	$g_{v(PMAPOSS)}$[f]	$g_{h(PMAPOSS)}$ = $g_{v(PMAPOSS)}$[g]	gh(PS) = $g_{v(PS)}$[h]	φ_{OR}[i] (deg)	$\sigma_{\varphi(OR)}$[j] (deg)	φ_{SL}[k] (deg)	$\sigma_{\varphi(SL)}$[l] (deg)
2.47	4.87	1.08	0.47	0.86	0.096	0.035	0.108	0.065	0.157	0.22	0	3.5	0	6.5

[a] Center-to-center distances of the PMAPOSS chain cylinders along *y*- and *z*-axis directions in the orthorhombic lattice (i.e., dimensions of the orthorhombic unit cell). [b] Average interdistance between the PMAPOSS block chains in amorphous phase. [c] Average interdistance between the amorphous PS block chains. [d] Radius of PMAPOSS chain cylinders. [e] Paracrystal distortion factors along *y*- and *z*-axis directions of the orthorhombic lattice structure. [f] Paracrystal distortion factors along *y*- and *z*-axis directions of the stacked PMAPOSS layer structure. [g] Paracrystal distortion factors of the PMAPOSS block chains in amorphous phase. [h] Paracrystal distortion factors of the amorphous PS block chains. [i] Orientation of the orthorhombic lattice structure with respect to the direction normal to the film plane. [j] Standard deviation in the orientation of the orthorhombic lattice structure. [k] Orientation of the molecularly stacked PMAPOSS layer structure with respect to the direction normal to the film plane. [l] Standard deviation in the orientation of the molecularly stacked PMAPOSS layer structure.

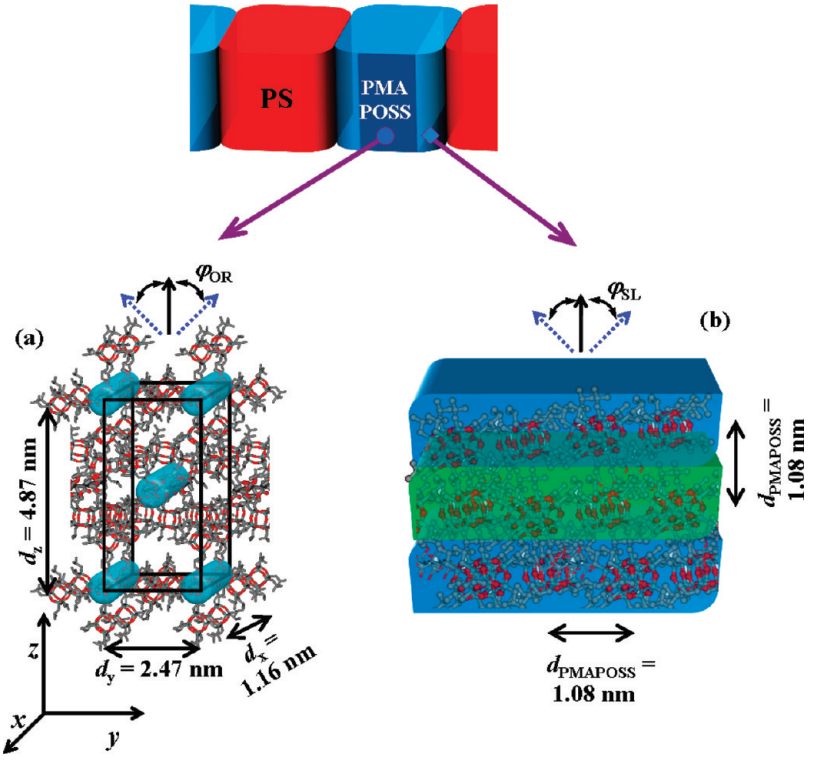

Figure 8. Schematic representation of the molecular packing structure of PMAPOSS domains in PS214-*b*-PMAPOSS27 films: (a) a densely ordered layer consisting of crystals in an orthorhombic lattice and (b) a less ordered layer composed of molecularly stacked layers.

that in the ordered domain the PMAPOSS chains have helical conformations and thus are present as molecular cylinders that lie parallel to the film plane and pack together laterally in the orthorhombic lattice.

In fact, the POSS units are bulky and thus difficult to align in a regular manner. Instead, they prefer to surround the polymer chain backbone of the PMAPOSS blocks in helical conformation, which results in a rod-like chain structure. The rod-like PMAPOSS block chains are organized into a hierarchical orthorhombic lattice structure as discussed above, which has dimensions of 4.87 nm perpendicular to the film plane and 2.47 nm parallel to the film plane. Since a face-centered orthorhombic lattice structure is formed, some peaks such as (00*l*) (*l* = odd) are forbidden and thus not observed. Although only a few peaks of the orthorhombic lattice are present, all the observed diffraction peaks are quite well matched with the lattice parameters of an orthorhombic lattice.

As discussed above, the GIWAXS results indicate that the phase-separated PMAPOSS domains consist of three different kinds of subphases, namely a molecularly stacked layer structure, orthorhombic crystals, and an amorphous phase. In comparison, the molecular packing density is higher in the orthorhombic crystal than in the molecularly stacked layer. Further, the molecularly stacked layer has a higher density than the amorphous phase. Thus, the orthorhombic crystals are mostly present in the densely ordered PMAPOSS layer (Figure 5b), which was identified with the GISAXS microstructure analysis discussed above, whereas the molecularly stacked layers are most probably present in the less ordered interfacial layer (Figure 5b). The amorphous phase might be present partially in both layers; however, the fraction of the amorphous phase is higher in the interfacial layer than in the densely ordered layer.

From the above structural information, a molecular packing model of the polymer chains in the densely ordered PMAPOSS domains (i.e., crystal layer) and in the less ordered PMAPOSS domains (i.e., interfacial layer) was developed and is shown in Figure 8.

To obtain structural details about the three subphases, we have attempted to quantitatively analyze the measured 2D GIWAXS pattern. First, the GIWAXS intensity from the orthorhombic lattice structure can be expressed by the form factor $P(\mathbf{q})$ and structure factor $S(\mathbf{q})$ of PMAPOSS block chains in helical conformation (i.e., molecular PMAPOSS cylinders), which are described in Appendix 2. The orientation of the paracrystal lattice in the orthorhombic structure was further considered as expressed in eqs 17−18 of Appendix 1. Using the GIXS formula (i.e., eq 1 in Appendix 1) with the form factor $P(\mathbf{q})$, structure factor $S(\mathbf{q})$ and orientation in Appendix 2, the GIWAXS from the orthorhombic

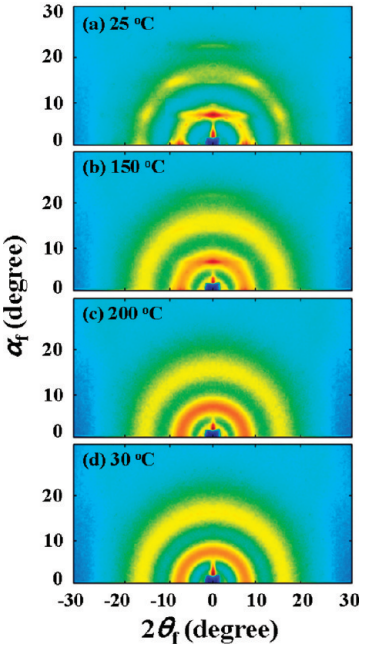

Figure 9. 2D GIWAXS patterns obtained with $\alpha_i = 0.150°$ for 70 nm thick PS_{214}-*b*-$PMAPOSS_{27}$ films deposited on silicon substrates at (a) 25, (b) 150, and (c) 200 °C during heating and (d) 30 °C during subsequent cooling.

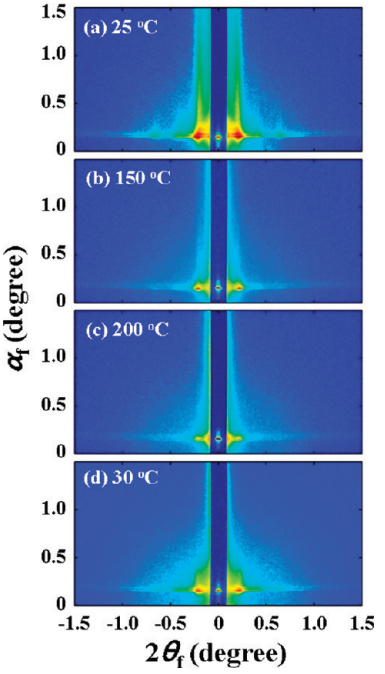

Figure 10. 2D GISAXS patterns obtained at $\alpha_i = 0.147°$ for 70 nm thick PS_{214}-*b*-$PMAPOSS_{27}$ films deposited on silicon substrates at (a) 25 °C, (b) 150 °C, and (c) 200 °C during heating and (d) 30 °C during cooling.

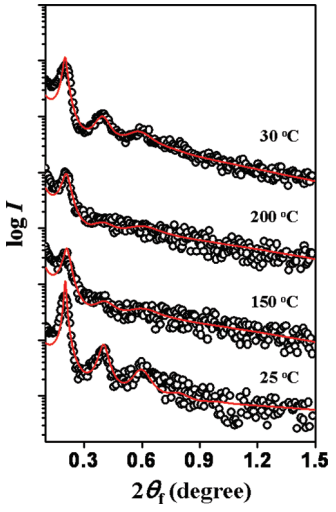

Figure 11. In-plane scattering profiles extracted from the 2D GISAXS patterns (Figure 10) along the $2\theta f$ direction at $\alpha_f = 0.160°$ during heating and subsequent cooling: the black symbols are the measured data and the red solid line was obtained by fitting the data with the GIXS formula.

structure of molecular PMAPOSS cylinders was analyzed in detail.

Second, the GIWAXS from the molecularly stacked layer structure of POSS units can be analyzed by using a two layer model based on paracrystals as reported previously in the literature.[22] In this analysis, the form factor $P(\mathbf{q})$, structure factor $S(\mathbf{q})$ and orientation described in Appendix 2 were used. In particular, it is noted that unlike the orientation of the lamellar microstructure found by the above GISAXS data analysis, the molecularly stacked layer structure of PMAPOSS chains has orientation distributed more along azimuthal direction as can be seen in the $\sigma_{\varphi(SL)}$ factor (i.e., the orientation of the molecularly stacked PMAPOSS layer structure with respect to the direction normal to the film plane) in Table 2; namely, the degree of orientation of the molecularly stacked PMAPOSS layer structure is relatively lower than that found for the lamellar structure by the GISAXS analysis. Using the GIXS formula (i.e., eq 1 in Appendix 1) with the form factor $P(\mathbf{q})$, structure factor $S(\mathbf{q})$ and orientation in Appendix 2, the GIWAXS from the molecularly stacked layer structure of POSS units was analyzed in detail.

Finally, we further attempted to analyze the amorphous halo rings from the amorphous region of the PMAPOSS domains and the amorphous PS domains in similar manner as described in Appendix 2 to analyze the GIWAXS from the molecularly stacked layer structure of POSS units. The amorphous halo ring centered at 17.8° originates from the amorphous PS domains and thus its *d*-spacing (0.47 nm) is assigned as d_{PS}. Another amorphous halo ring centered at 7.35° comes from the amorphous region of the PMAPOSS domains and its *d*-spacing (1.08 nm) is assigned as $d_{PMAPOSS}$. The orientation of the paracrystal lattices in the amorphous PS domains and the amorphous PMAPOSS phase are considered fully isotropic along azimuthal direction. Using the GIXS formula (eq 1 in Appendix 1) with the form factor $P(\mathbf{q})$, structure factor $S(\mathbf{q})$ and orientation in Appendix 2, the GIWAXS data from the amorphous PS domains and the amorphous phase of the PMAPOSS domains were analyzed in detail.

As shown in parts c and d of Figure 7, the in-plane scattering profile (which was extracted along the $2\theta_f$ direction at $\alpha_f = 0.30°$), as well as the out-of-plane scattering profile (which was extracted along the α_f direction at $2\theta_f = 0.0°$) can be satisfactorily fitted with the GIXS formula derived in Appendix 2 for the orthorhombic lattice structure of PMAPOSS chains, the molecularly stacked layer structure of POSS units (i.e., PMAPOSS chains), and the amorphous PS domains and PMAPOSS phase in the film, which confirms that the measured GIWAXS pattern was successfully analyzed. In this analysis, the scattering intensity of each scatterer system was independently acquired and then linearly added to obtain the full scattering profile. From this quantitative analysis with the GIXS formula, the structural parameters have been obtained and summarized in Table 2. Furthermore, the 2D GIWAXS pattern was reconstructed from the acquired structural

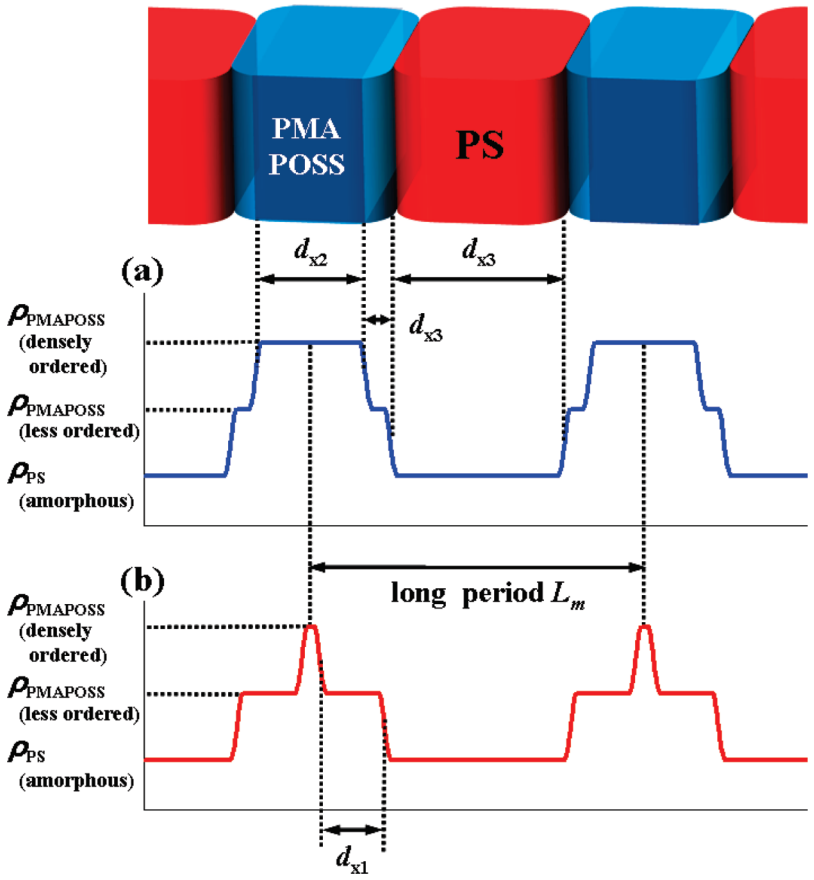

Figure 12. Relative electron density profile along the long period of the lamellar structure formed in the PS_{214}-*b*-$PMAPOSS_{27}$ film supported on a silicon substrate: (a) 25 °C before heating; (b) 200 °C on heating. Here, d_{x1}, d_{x2}, and d_{x3} are the thicknesses of the less ordered PMAPOSS layer, the densely ordered PMAPOSS layer, and the amorphous PS layer, respectively.

parameters by using the GIXS formula. The reconstructed 2D GIWAXS pattern is displayed in Figure 7e, and is in good agreement with the measured 2D GIWAXS pattern shown in Figure 7a.

The GIWAXS and GISAXS measurements were further conducted in situ during heating and subsequent cooling of the diblock copolymer film. Figure 9 shows representative 2D GIWAXS patterns obtained during heating and subsequent cooling. On heating, the 2D GIWAXS pattern was found to vary slightly in intensity up to around 170 °C (Figure 9b). However, in the range 170−190 °C the intensity of the scattering pattern varies significantly with increasing temperature (data not shown). Above 190 °C, the scattering characteristics of the orthorhombic crystal lattice and the ordered layers disappear completely and only two representative amorphous halo rings are present (Figure 9c), which confirms the complete destruction of the structures in the film. These in situ GIWAXS measurements confirm that the orthorhombic lattice and the molecularly stacked layer structures formed in the film are retained up to around 170 °C, undergo a melting transition in the range 170−190 °C, and are completely melted above 190 °C. The destruction of the structures is also evident in the DSC thermogram (Figure 3B), as discussed above.

In-situ GIWAXS measurements were also conducted for the films during subsequent cooling after heating. Figure 9d shows a representative scattering pattern obtained during cooling: it contains only two amorphous halo rings, and is quite different from that obtained before heating. These scattering results indicate that the orthorhombic lattice and molecularly stacked layer structures in the thermally annealed films do not form easily during the cooling process; thus the formation of these structures requires additional treatment such as thermal annealing.

Figure 10 shows representative 2D GISAXS patterns obtained during heating and subsequent cooling. Further, in-plane scattering profiles were extracted from the 2D GISAXS patterns along the $2\theta_f$ direction at $\alpha_f = 0.17°$, and are displayed in Figure 11. The in-plane scattering profiles acquired at various temperatures can be satisfactorily fitted with the GIXS formula derived above for the multilayer structures in thin films (Figure 11), which confirms that the in situ measured GISAXS patterns were successfully analyzed. The obtained structural parameters are summarized in Table 1.

As can be seen in Figures 10 and 11, the GISAXS pattern obtained during heating is well retained up to 150 °C, although the intensities of the higher order scattering spots weaken with increasing temperature. Upon further heating to 200 °C, the first order scattering spot of the lamellar structure is still retained but the higher order scattering spots weaken significantly (Figures 10 and 11). This GISAXS pattern was found to persist up to 320 °C, which is near the degradation temperature of the polymer (data not shown). However, the intensities of the higher order scattering spots were found to return during subsequent cooling after heating (Figures 10 and 11). These GISAXS results confirm that the lamellar structure (which is composed of the phase-separated PS and PMAPOSS domains) developed in the diblock copolymer films is retained below the degradation temperature of the diblock copolymer without any discernible order-to-disorder transition and that the degree of ordering of the lamellar structure is somewhat degraded with increasing temperature during the heating run, which may be due to the thermally induced mobilization of the polymer block chains in the individual layers of the lamellar structure. The thermally induced degradation of the ordering in the lamellar structure is also evident in the positional

distortion factor (i.e., *g*-factor). As can be seen in Table 1, the g_1-factor (that is the *g*-factor along the direction normal to the lamellar plane) was determined to be 0.098 at 25 °C but increases to 0.164 at 150 °C and further increases to 0.176 at 200 °C. On subsequent cooling, the g_1-factor returns to a low value, 0.118 at 30 °C. Further, the in situ GISAXS analysis shows that during heating and subsequent cooling the thicknesses of the densely ordered and less ordered PMAPOSS layers in the lamellar structure vary significantly with temperature, which is attributed to the melting and reformation of the orthorhombic crystals and the molecularly stacked layer structure in the PMAPOSS domains (Figure 12).

The above GIXS analyses confirm both the coexistence of phase-separated PS and PMAPOSS domains and the presence of crystals indicated in the DSC measurement. In particular, the in situ GIWAXS analysis confirms that the weak, broad endothermic peak around 173 °C (Figure 3B) originates from melting of the orthorhombic and molecularly layered crystals formed in the PMAPOSS domains. The weak and broad nature of the melting endothermic peak might be attributed to several possible factors as follows. The first considerable factor is the coexistence of orthorhombic crystals, molecularly layered crystals and amorphous phase in the PMAPOSS domain; the presence of the two different types of crystals causes the melting peak broader and weaker while the portion of amorphous phase may also contribute negatively to the melting endothermic peak. The second possible factor is a limited ordering length in both the two different types of crystals; shorter ordering length causes melting endothermic peak broader and weaker. The third possible factor is the bulkiness and helical conformation of the PMAPOSS block discussed above. Such the bulkiness and chain conformation may lead the formation of relatively low density of crystals, which have low cohesive energy and thus reveal low heat of fusion in melting, consequently showing weak endothermic peak.

Conclusions

The morphological structures in nanoscale thin films of PS_{214}-*b*-$PMAPOSS_{27}$, an interesting diblock copolymer containing POSS moieties, were investigated in detail at various temperatures by using in situ GIXS (GISAXS and GIWAXS) with a synchrotron radiation source. GIXS formulas based on structural models were derived in order to perform quantitative analyses of the 2D GISAXS and GIWAXS data. In addition, the thermal properties of the diblock copolymer were characterized with DSC analysis: T_g = 96 °C (amorphous PS phase); T_m = 173 °C (PMAPOSS crystals); T_g of the amorphous PMAPOSS phase could not be detectable because of the very weak nature of glass transition). The quantitative 2D GIXS analyses found the following structural details and their variations with temperature during heating and cooling.

The diblock copolymer molecules in the thin films undergo phase separation into PS and PMAPOSS domains. Surprisingly, the phase-separated PS and PMAPOSS domains are stacked together alternately as layers along the film plane, forming a lamellar structure perfectly oriented in the out-of-plane of the film; the thicknesses of the PS and PMAPOSS domain layers are 20.4 and 15.9 nm, respectively. Such the vertically oriented lamellar structure was favorably formed in the solvent-annealed films with and without further thermal annealing. In comparison, randomly oriented lamellar structure was found to form in the thermally annealed films. In the lamellar structure, the PMAPOSS layers are composed of two sublayers, namely a densely ordered layer (13.0 nm thick) and a less ordered layer (2.9 nm thick). The block chains in the densely ordered layer form orthorhombic crystals whereas those in the less ordered layer form molecularly stacked layers. Both the orthorhombic PMAPOSS crystals and the molecularly stacked PMAPOSS layers are also oriented in the out-of-plane of the film. The formation of the crystals and ordered layers might be induced by the ordering ability of the POSS moieties. Furthermore, the PMAPOSS block chains have helical conformations and thus are present as molecular cylinders, which make the formation of the crystals and ordered layers possible. It was also found that a certain fraction of the amorphous phase is present in both the densely ordered layer and the less ordered layer.

This vertically oriented lamellar structure is very stable and thus well retained without any order-to-order or order-to-disorder phase transition below the degradation temperature (330 °C) of the polymer. However, on heating the orthorhombic crystals and the molecularly stacked layers in the PMAPOSS domains were found to melt over the range 170−190 °C. Because of melting, both the thicknesses and densities of the densely ordered and less ordered PMAPOSS layers in the lamellar structure vary significantly with temperature. During the subsequent cooling run, the orthorhombic crystals and molecularly stacked layers are not fully recovered, which indicates that the formation of orthorhombic crystals and stacked layers in the PMAPOSS domains requires thermal annealing.

For the phase-separated lamellar structure as well as the orthorhombic crystal lattice and ordered layers in the PMAPOSS domains, detailed structural parameters were determined. From the determined structural parameters, 2D GISAXS and GIWAXS patterns were reconstructed by using the GIXS formulas, and found to be in good agreement with the experimental patterns. Furthermore, a hierarchical structure model of thin films of the diblock copolymer was developed by considering the determined structural parameters.

Acknowledgment. This study was supported by the National Research Foundation of Korea (Center for Electro-Photo Behaviors in Advanced Molecular Systems) and by the Ministry of Education, Science & Technology (MEST) (BK21 Program and World Class University Program). The synchrotron GIXS measurements at Pohang Accelerator Laboratory were supported by MEST, POSCO and POSTECH Foundation. T.H. acknowledges the Mitsubishi Chemical Corporation Fund. P.G. acknowledges partial support from the UW-NSF Nanoscale Science and Engineering Center (DMR-0832760).

Appendix 1

The intensity of GIXS (I_{GIXS}) can be expressed by the scattering formula derived recently:[5,6,16,17]

$$I_{GIXS}(\alpha_f, 2\theta_f) \cong \frac{1}{16\pi^2} \times \frac{1-e^{-2\mathrm{Im}(q_z)d}}{2\mathrm{Im}(q_z)} \begin{bmatrix} |T_i T_f|^2 I_1(q_{||}, \mathrm{Re}(q_{1,z})) + \\ |T_i R_f|^2 I_1(q_{||}, \mathrm{Re}(q_{2,z})) + \\ |T_f R_i|^2 I_1(q_{||}, \mathrm{Re}(q_{3,z})) + \\ |R_i R_f|^2 I_1(q_{||}, \mathrm{Re}(q_{4,z})) \end{bmatrix} \quad (1)$$

where $\mathrm{Im}(q_z) = |\mathrm{Im}(k_{z,f})| + |\mathrm{Im}(k_{z,i})|$, $\mathrm{Re}(x)$ is the real part of x, d is the film thickness, R_i and T_i are the reflected and transmitted amplitudes of the incoming X-ray beam respectively, and R_f and T_f are the reflected and transmitted amplitudes of the outgoing X-ray beam, respectively. In addition,

$$q_{||} = \sqrt{{q_x}^2 + {q_y}^2}$$

$q_{1,z} = k_{z,f} - k_{z,i}$, $q_{2,z} = -k_{z,f} - k_{z,i}$, $q_{3,z} = k_{z,f} + k_{z,i}$, and $q_{4,z} = -k_{z,f} + k_{z,i}$; here, $k_{z,i}$ is the z-component of the wave vector of

the incoming X-ray beam, which is given by

$$k_{z,\mathrm{i}} = k_{\mathrm{o}}\sqrt{{n_{\mathrm{R}}}^2 - \cos^2 \alpha_{\mathrm{i}}}$$

and $k_{z,\mathrm{f}}$ is the z-component of the wave vector of the outgoing X-ray beam, which is given by

$$k_{z,\mathrm{f}} = k_{\mathrm{o}}\sqrt{{n_{\mathrm{R}}}^2 - \cos^2 \alpha_{\mathrm{f}}}$$

where $k_{\mathrm{o}} = 2\pi/\lambda$, λ is the wavelength of the X-ray beam, n_{R} is the refractive index of the film given by $n_{\mathrm{R}} = 1 - \delta + i\xi$ with dispersion δ and absorption ξ, α_{i} is the out-of-plane grazing incident angle of the incoming X-ray beam, and α_{f} is the out-of-plane exit angle of the out-going X-ray beam. q_x, q_y, and q_z are the components of the scattering vector $\mathbf{q}$. I_1 is the scattering intensity of the structure in the film, which can be calculated kinematically.

In eq 1, I_1 is the scattered intensity from the layer structures in the film, and thus can be expressed by the following equation:[5,6,16,17,23]

$$I_1(\mathbf{q}) = P(\mathbf{q})\cdot S(\mathbf{q}) \tag{2}$$

where $P(\mathbf{q})$ is the form factor of the scatterers that describes the shape, size, and orientations of the layer structures, and $S(\mathbf{q})$ is the structure factor that provides information on the positions of the layer structures such as the crystal lattice parameters, orientation, dimension, and symmetry in an ordered structure and the interdistance of the layer structures. The form factor $P(\mathbf{q})$ for such the multilayer structure with three different scattering length densities ($\overline{b1}$ for less ordered (i.e., less dense) PMAPOSS layer, $\overline{b2}$ for ordered (i.e., dense) PMAPOSS layer, and $\overline{b3}$ for the amorphous PS layer) can be expressed as follows:[24,25]

$$P(\mathrm{q}) = \left[\frac{\tilde{b1}^2}{{q_z}^2}\,\mathrm{Re}[ib(q_z)] + \frac{\overline{b2}^2}{{q_y}^2}\,\mathrm{Re}\left[\frac{(1-Y_1)(1-Y_2)}{(1-Y_1Y_2)}\right] + \frac{\overline{b3}^2}{{q_x}^2}\,\mathrm{Re}\left[\frac{(1-X_1)(1-X_2)}{(1-X_1X_2)}\right]\right] \tag{3}$$

with

$$ib(q_z) = \left|\left[\frac{(1-F_3)(1-{F_1}^2F_2) + (\tilde{br}-1)^2(1-F_2)(1-{F_1}^2F_3)}{1-{F_1}^2F_2F_3}\right] + \left[\frac{2(\tilde{br}-1)F_1(1-F_3)(1-F_2)}{1-{F_1}^2F_2F_3}\right]\right| \tag{4}$$

where

$$\tilde{b}_1 = (\overline{b_1} - \overline{b_3})\exp(-(1/2){q_z}^2{\sigma_{\mathrm{int}\,1}}^2) \tag{5a}$$

$$\tilde{b}2 = (\overline{b_2} - \overline{b_3})\exp(-(1/2){q_z}^2{\sigma_{\mathrm{int}\,2}}^2) \tag{5b}$$

and

$$\tilde{br} = \tilde{b}_2/\tilde{b}_1 \tag{5c}$$

The scattering length densities given above are the relative values with respect to $\overline{b_3}$, according to the Babinet principle. $\sigma_{\mathrm{int}\,1}$ and $\sigma_{\mathrm{int}\,2}$ are the diffuse boundaries. F_{k}, Y_{k}, and X_{k} are the Fourier transform of the Gaussian distribution function of thickness $d_{z\mathrm{k}}$, $d_{y\mathrm{k}}$, and $d_{x\mathrm{k}}$, which are defined by

$$F_k(q) = \exp(-iqd_{zk} - (1/2){q_z}^2{\sigma_{zk}}^2) \tag{6a}$$

$$Y_k(q) = \exp(-iqd_{yk} - (1/2){q_y}^2{\sigma_{yk}}^2) \tag{6b}$$

$$X_k(q) = \exp(-iqd_{xk} - (1/2){q_x}^2{\sigma_{xk}}^2) \tag{6c}$$

Here the lamellar long period is defined by $L_m = 2d_{x1} + d_{x2} + d_{x3}$ (see the structural model in Figure 5b).

For a paracrystal model,[26] the structure factor $S(\mathbf{q})$, which is also known as the interference function or lattice factor, can be determined from the Fourier transform of a complete set of lattice points. In the paracrystal model with distortion of the second kind, its lattice points are no longer fixed at certain positions but instead are described by a positional distribution function. In the simple case where the autocorrelation function of a crystal lattice is given by the convolution product of the distributions of the lattice points along three axes and the distribution function is a Gaussian, $S(\mathbf{q})$ can be expressed by the following equation:

$$S(\mathbf{q}) = \prod_{k=1}^{3} Z_k(\mathbf{q}) \tag{7}$$

$$Z_k(\mathbf{q}) = 1 + \frac{F_k(\mathbf{q})}{1-F_k(\mathbf{q})} + \frac{F_k^*(\mathbf{q})}{1-F_k^*(\mathbf{q})} \tag{8}$$

$$F_k(\mathbf{q}) = |F_k(\mathbf{q})|\mathrm{e}^{-i\mathbf{q}\cdot\mathbf{a}_k} \tag{9}$$

$$\left|F_k(\mathbf{q})\right| = \exp\left[-\left(\frac{{q_1}^2{g_1}^2 + {q_2}^2{g_2}^2 + {q_3}^2{g_3}^2}{2}\right)\right] \tag{10}$$

Here $\mathbf{a_k}$ is the k component of the fundamental vector $\mathbf{a}$ of the multilayer structure, which are defined as:

$$\mathbf{a_1} = L_m\cdot\mathbf{b_1} \tag{11a}$$

$$\mathbf{a_2} = L_s\cdot\mathbf{b_2} \tag{11b}$$

$$\mathbf{a_3} = L_z\cdot\mathbf{b_3} \tag{11c}$$

where L_m, L_s and L_z are the dimensions of the lamellar structure unit along the x, y, and z directions respectively; $\mathbf{b_1}$, $\mathbf{b_2}$, and $\mathbf{b_3}$ are the unit vectors on x, y, and z direction, respectively. g_1, g_2, and g_3 are the components of the paracrystal distortion factor g, which are defined by

$$g_1 = \Delta\mathbf{a_1}/\mathbf{a}_1 \tag{12a}$$

$$g_2 = \Delta\mathbf{a_2}/\mathbf{a}_2 \tag{12b}$$

$$g_3 = \Delta\mathbf{a_3}/\mathbf{a}_3 \tag{12c}$$

where $\Delta\mathbf{a_k}$ is the displacement of the vector $\mathbf{a_k}$. In this case, the isotropic displacement is assumed and the domain orientation is accounted for numerically. q_1, q_2, and q_3 are the components of the scattering vector $\mathbf{q}$, which are defined as:

$$q_1 = \mathbf{a_1}\cdot\mathbf{q}_x + \mathbf{a_1}\cdot\mathbf{q}_y + \mathrm{a_1}\cdot\mathbf{q}_z \tag{13a}$$

$$q_2 = \mathbf{a_2}\cdot\mathbf{q}_x + \mathbf{a_2}\cdot\mathbf{q}_y + \mathbf{a_2}\cdot\mathbf{q}_z \tag{13b}$$

$$q_3 = \mathbf{a_3}\cdot\mathbf{q}_x + \mathbf{a_3}\cdot\mathbf{q}_y + \mathbf{a_3}\cdot\mathbf{q}_z \tag{13c}$$

From eqs 7−13 with the fundamental vectors, the structure factor $S(\mathbf{q})$ can be determined by using various paracrystal distortion

factors g, and also d-spacing values of the diffraction planes determined.

Moreover, for a structure with a given orientation in a film, its fundamental vectors can be rotated and transformed by a rotation matrix. When the structure of the film is randomly oriented in the plane of the film but uniaxially oriented out of plane, the peak position vector $\mathbf{q_c}$ of a certain reciprocal lattice point $\mathbf{c}^*$ in the sample reciprocal lattice is given by

$$\begin{aligned} \mathbf{q_c} &= \mathbf{R}\cdot\mathbf{c}^* \\ &\equiv (q_{c,x}, q_{c,y}, q_{c,z}) \end{aligned} \tag{14}$$

where $\mathbf{R}$ is a 3×3 matrix to decide the preferred orientation of the structure in the film, and $q_{c,x}$, $q_{c,y}$, and $q_{c,z}$ are the x, y, z components of the peak position vector $\mathbf{q_c}$, respectively. Using eq 13, every peak position can be obtained. Because of cylindrical symmetry, the Debye−Scherrer ring composed of the in-plane randomly oriented $\mathbf{c}^*$ cuts an Ewald sphere at two positions in its top hemisphere:

$$q_{||} = q_{c,||} \equiv \pm\sqrt{{q_{c,x}}^2 + {q_{c,y}}^2}$$

with $q_z = q_{c,z}$. Thus, diffraction patterns with cylindrical symmetry are easily calculated in the **q**-space. It is then convenient to determine the preferred orientation of known structures and further to analyze anisotropic X-ray scattering patterns. However, since **q**-space is distorted in GIXS by refraction and reflection effects, the relation between the detector plane expressed as the Cartesian coordinate defined by two perpendicular axes (i.e., by the in-plane exit angle $2\theta_f$ and the out-of-plane exit angle α_f) and the reciprocal lattice points is needed. The two wave vectors $k_{z,i}$ and $k_{z,f}$ are corrected for refraction as

$$k_{z,i} = k_o\sqrt{{n_R}^2 - \cos^2\alpha_i}$$

and

$$k_{z,f} = k_o\sqrt{{n_R}^2 - \cos^2\alpha_f}$$

respectively. Therefore, the two sets of diffractions that result from the incoming and outgoing X-ray beams, and denoted by q_1 and q_3 respectively, are given at the exit angles by the following expression:

$$\alpha_f = \arccos\left(\sqrt{{n_R}^2 - \left(\frac{q_{c,z}}{k_o} \pm \sqrt{{n_R}^2 - \cos^2\alpha_i}\right)^2}\right) \tag{15}$$

where

$$q_{c,z}/k_o > \sqrt{{n_R}^2 - \cos^2\alpha_i}$$

In eq 15, the positive sign denotes diffractions produced by the outgoing X-ray beam, and the negative sign denotes diffractions produced by the incoming X-ray beam. The in-plane incidence angle $2\theta_i$ is usually zero, so the in-plane exit angle $2\theta_f$ can be expressed as follows:

$$2\theta_f = \arccos\left(\frac{\cos^2\alpha_i + \cos^2\alpha_f - \left(\frac{q_{c,||}}{k_o}\right)^2}{2\cos\alpha_i\cos\alpha_f}\right) \tag{16}$$

Therefore, diffraction spots detected on the detector plane in GIXS measurements can be directly compared to those derived using eqs 14−16 from an appropriate model and thus analyzed in terms of the model.

To obtain information on the orientation of the paracrystal lattice in the multilayer structure from GIXS data, the distribution of the orientation vector $\mathbf{n}$ is given by a function $D(\varphi)$, where φ is the polar angle between the $\mathbf{n}$ vector and the out-of-plane of the film (Figure 5c); for example, φ is zero when the $\mathbf{n}$ vector in the film is oriented normal to the film plane. To calculate the 2D GIXS patterns, $D(\varphi)$ should be represented by a numerical function. In relation to the distribution of the lattice orientation, $D(\varphi)$ can generally be considered as a Gaussian distribution:

$$D(\varphi) = \frac{1}{\sqrt{2\pi}\sigma_\varphi}\exp\left[-\frac{(\varphi - \overline{\varphi})^2}{2{\sigma_\varphi}^2}\right] \tag{17}$$

where $\overline{\varphi}$ and σ_φ are the mean angle and standard deviation of φ from $\overline{\varphi}$, respectively. The observed scattering intensity $I_{GIXS,\varphi}(\mathbf{q})$ is obtained by averaging $I_{GIXS}(\mathbf{q})$ over possible orientations of the lattice:

$$I_{GIXS,\varphi}(\mathbf{q}) = \int_{-\pi}^{\pi} I_{GIXS}(\mathbf{q})D(\varphi)\,\mathrm{d}\varphi \tag{18}$$

Appendix 2

The GIWAXS intensity from the orthorhombic lattice structure can be expressed by the GIXS formula (eq 1 in Appendix 1) with the form factor $P(\mathbf{q})$ and structure factor $S(\mathbf{q})$ of PMAPOSS block chains in helical conformation (i.e., molecular PMAPOSS cylinders). The form factor $P(\mathbf{q})$ of the molecular PMAPOSS cylinder with radius R and length L can be expressed by the following equation:[6,18]

$$P(\mathbf{q}) = F^2(\mathbf{q}, R, L) \tag{19}$$

where $F(\mathbf{q}, R, L)$ is the structure amplitude of the cylindrical scatterer oriented normal to the film plane given by

$$F(\mathbf{q}, R, L) = 2\pi R^2 L\frac{J_1(q_{||}R)}{q_{||}R}\frac{\sin(q_zL/2)}{q_zL/2}\exp(-iq_zL/2) \tag{20}$$

where $q_{||} = ({q_x}^2 + {q_y}^2)^{1/2}$. Here also it is assumed that the distribution of the radius R of the cylinders follows a Gaussian size distribution function $G(R)$:

$$G(R) = \frac{1}{\sqrt{2\pi}\sigma_\varphi}\exp\left[-\frac{(R - \overline{R})^2}{2{\sigma_R}^2}\right] \tag{21}$$

where $\overline{R}$ and σ_R are the mean radius and a standard deviation of R from $\overline{R}$, respectively. The size distribution of the cylinders can be taken into account by averaging the form factor $\langle F\rangle$ with respect to R, yielding

$$\langle F\rangle = \frac{\int_0^\infty G(R)F(\mathbf{q}, R, L)\,\mathrm{d}R}{\int_0^\infty G(R)\,\mathrm{d}R} \tag{22}$$

The structure factor $S(\mathbf{q})$ of the orthorhombic lattice was derived from paracrystal model using eqs 7−10 in Appendix 1. However, in eq 9, $\mathbf{a_k}$ is again defined for the orthorhombic structure as follows:

$$\mathbf{a_1} = d_x\cdot\mathbf{b_1} \tag{23a}$$

$$\mathbf{a_2} = d_y\cdot\mathbf{b_2} \tag{23b}$$

$$\mathbf{a_3} = d_z\cdot\mathbf{b_3} \tag{23c}$$

where d_x, d_y, and d_z are the dimensions of orthorhombic lattice on x, y, and z-axis direction, and $\mathbf{b}_1$, $\mathbf{b}_2$, and $\mathbf{b_3}$ are the unit vectors in the x, y, and z directions in the film plane. Further, the g_x, g_y, and g_3 components of the paracrystal distortion factor g are defined in similar manner as defined in eq 12 of Appendix 1:

$$g_x = \Delta\mathbf{a_1}/\mathbf{a_1} \tag{24a}$$

$$g_y = \Delta\mathbf{a_2}/\mathbf{a_2} \tag{24b}$$

$$g_z = \Delta\mathbf{a_3}/\mathbf{a_3} \tag{24c}$$

In the data analysis, the distortion factor g_x was regardless because it is along the cylindrical PMAPOSS block chain but the other two distortion factors were considered.

The orientation of the paracrystal lattice in the orthorhombic structure was further considered as expressed in eqs 17−18 (Appendix 1).

On the other hand, the GIWAXS from the molecularly stacked layer structure of POSS units can be analyzed by using eqs 1 and 2 (Appendix 1) for a two layer model based on paracrystals as reported previously in the literature.[22] In this analysis, the form factor $P(\mathbf{q})$ of POSS units, whose lattice dimensions are L_1, L_2, and L_3, can be expressed as the following equation:

$$P(\mathbf{q}) = \exp\left\{\frac{1}{4\pi}[{L_1}^2(q_x \sin\beta + q_z \cos\beta)^2 + L_2{q_y}^2 + L_3{q_z}^2]\right\}\sin^2\beta \tag{25}$$

where β is the angle between the $\mathbf{a_1}$ and $\mathbf{a_3}$ components of the lattice vector $\mathbf{a}$. In this study, the lattice dimensions are assumed to be identical to the interdistance (d_{PMAPOSS}) between the POSS units (i.e., PMAPOSS chains) in the molecularly layer structure: namely, $L_1 = L_2 = L_3 = d_{\mathrm{PMAPOSS}}$. The structure factors $S(\mathbf{q})$ can also be considered as paracrystal model in the following equation:

$$S(\mathbf{q}) = [\langle|f|^2\rangle - |\langle f\rangle^2|] + |\langle f\rangle^2|[\prod_{\mathrm{k}=1}^{3} Z_{\mathrm{k}}(\mathbf{q})] \tag{26}$$

where

$$f = \frac{\sin(q_z h/2)}{q_z h/2}\exp(-{\sigma_h}^2{q_z}^2/2) \tag{27}$$

In the above equation, $h = d_{\mathrm{POSS}}$ and σ_h is its deviation. The k-th lattice factor $Z_{\mathrm{k}}(\mathbf{q})$ is given by:

$$Z_{\mathrm{k}}(\mathbf{q}) = \frac{1 - |F_{\mathrm{k}}(\mathbf{q})|^2}{1 + |F_{\mathrm{k}}(\mathbf{q})|^2 - 2|F_{\mathrm{k}}(\mathbf{q})|\cos(\mathbf{q}\cdot\mathrm{a_k})} \tag{28}$$

where

$$F_1(\mathbf{q}) = F_2(\mathbf{q}) = F_3(\mathbf{q}) = \exp\left[-\left(\frac{{q_r}^2 h^2 {g_h}^2 + {q_z}^2 h^2 {g_v}^2}{2}\right)\right] \tag{29}$$

and

$$\mathbf{q}\cdot\mathbf{a_1} = (q_x + q_z \cot\beta)h \tag{30a}$$

$$\mathbf{q}\cdot\mathbf{a_2} = q_y h \tag{30b}$$

$$\mathbf{q}\cdot\mathbf{a_3} = q_z h \tag{30c}$$

where $\mathbf{a_k}$ is the fundamental vector of the k-th axis and

$$q_r = \sqrt{{q_x}^2 + {q_y}^2}$$

g_{h} and g_{v} are the components of the paracrystal distortion factor, which are defined as:

$$g_{\mathrm{h}} = \Delta a_{\mathrm{h}}/a_{\mathrm{r}} \tag{31a}$$

$$g_{\mathrm{v}} = \Delta a_{\mathrm{v}}/a_{\mathrm{r}} \tag{31b}$$

where Δa_{h} represents the displacement of the fundamental vector $\mathbf{a_1}$ and $\mathbf{a_2}$ parallel to the film plane and Δa_{v} represents the displacement of the fundamental vector $\mathbf{a_3}$ perpendicular to the film plane. The orientation of the paracrystal lattice in the molecularly stacked layer structure is further considered as expressed in eqs 17 and 18 (Appendix 1).

References and Notes

(1) (a) Liu, Y.; Zhao, W.; Zheng, X.; King, A.; Singh, A.; Rafailovich, M. H.; Sokolov, J.; Dai, K. H.; Kramer, E. J.; Schwarz, S. A.; Gebizlioglu, O.; Sinha, S. K. *Macromolecules* **1994**, *27*, 4000. (b) Park, M.; Harrison, C.; Chaikin, P. M.; Register, R. A.; Adamson, D. H. *Science* **1997**, *276*, 1401. (c) Mansky, P.; Russell, T. P.; Hawker, C. J.; Pitsikalis, M.; Mays, J. *Macromolecules* **1997**, *30*, 6810. (d) Kim, G.; Libera, M. *Macromolecules* **1998**, *31*, 2569. (e) Elbs, H.; Fukunaga, K.; Stadler, R.; Sauer, G.; Magerle, R.; Krausch, G. *Macromolecules* **1999**, *32*, 1204. (f) Yokoyama, H.; Mates, T. E.; Kramer, E. J. *Macromolecules* **2000**, *33*, 1888.

(2) (a) Fasolka, M. J.; Mayes, A. M. *Annu. Rev. Mater. Res.* **2001**, *31*, 323. (b) Segalman, R. A.; Yokoyama, H.; Kramer, E. J. *Adv. Mater.* **2001**, *13*, 1152. (c) Guarini, K. W.; Black, C. T.; Yeung, S. H. I. *Adv. Mater.* **2002**, *14*, 1290. (d) Krausch, G.; Magerle, R. *Adv. Mater.* **2002**, *14*, 1579. (e) Tian, Y.; Watanabe, K.; Kong, X.; Abe, J.; Iyoda, T. *Macromolecules* **2002**, *35*, 3739. (f) Knoll, A.; Horvat, A.; Lyakhova, K. S.; Krausch, G.; Sevink, G. J. A.; Zvelindovsky, A. V.; Magerle, R. *Phys. Rev. Lett.* **2002**, *89*, 035501. (g) Sohn, B. H.; Yun, S. H. *Polymer* **2002**, *43*, 2507.

(3) (a) Kim, S. O.; Solak, H. H.; Stoykovich, M. P.; Ferrier, N. J.; de Pablo, J. J.; Nealey, P. F. *Nature* **2003**, *424*, 411. (b) Xu, T.; Stevens, J.; Villa, J.; Goldbach, J. T.; Guarini, K. W.; Black, C. T.; Hawker, C. J.; Russell, T. P. *Adv. Funct. Mater.* **2003**, *13*, 698. (c) Segalman, R. A.; Hexemer, A.; Kramer, E. J. *Macromolecules* **2003**, *36*, 18. (d) Park, C.; Yoon, J.; Thomas, E. L. *Polymer* **2003**, *44*, 6725. (e) Jeong, U.; Ryu, D. Y.; Kho, D. H.; Lee, D. H.; Kim, J. K.; Russell, T. P. *Macromolecules* **2003**, *36*, 3626. (f) Jeong, U.; Ryu, D. Y.; Kho, D. H.; Kim, J. K.; Goldbach, J. T.; Kim, D. H.; Russell, T. P. *Adv. Mater.* **2004**, *16*, 533. (g) Angelescu, D. E.; Waller, J. H.; Adamson, D. H.; Deshpande, P.; Chou, S. Y.; Register, R. A.; Chaikin, P. M. *Adv. Mater.* **2004**, *16*, 1736. (h) Kim, S. H.; Misner, M. J.; Xu, T.; Kimura, M.; Russell, T. P. *Adv. Mater.* **2004**, *16*, 226. (i) Xu, T.; Goldbach, J. T.; Misner, M. J.; Kim, S.; Gibaud, A.; Gang, O.; Ocko, B.; Guarini, K. W.; Black, C. T.; Hawker, C. J.; Russell, T. P. *Macromolecules* **2004**, *37*, 2972.

(4) (a) Park, I.; Lee, B.; Ryu, J.; Im, K.; Yoon, J.; Ree, M.; Chang, T. *Macromolecules* **2005**, *38*, 10532. (b) Park, I.; Park, S.; Park, H.-W.; Chang, T.; Yang, H.; Ryu, C. Y. *Macromolecules* **2006**, *39*, 315. (c) Bang, J.; Kim, S. H.; Drockenmuller, E.; Misner, M. J.; Russell, T. P.; Hawker, C. J. *J. Am. Chem. Soc.* **2006**, *128*, 7622. (d) Yun, S.-H.; Sohn, B.-H.; Jung, J. C.; Zin, W.-C.; Ree, M.; Park, J. W. *Nanotechnology* **2006**, *17*, 450. (e) Chung, B.; Choi, M.; Ree, M.; Jung, J. C.; Zin, W.-C.; Chang, T. *Macromolecules* **2006**, *39*, 684. (f) Im, K.; Park, H.-W.; Kim, Y.; Chung, B.; Ree, M.; Chang, T. *Anal. Chem.* **2007**, *79*, 1067. (g) Park, H.-W.; Im, K.; Chung, B.; Ree, M.; Chang, T.; Sawa, K.; Jinnai, H. *Macromolecules* **2007**, *40*, 2603. (h) Son, J. G.; Bulliard, X.; Kang, H.; Nealey, P. F.; Char, K. *Adv. Mater.* **2008**, *20*, 3643. (i) Jo, P. S.; Sung, J.; Park, C.; Kim, E.; Ryu, D. Y.; Pyo, S.; Kim, H.-C.; Hong, J. M. *Adv. Funct. Mater.* **2008**, *18*, 1202. (j) Chung, B.; Choi, H.; Park, H.-W.; Ree, M.; Jung, J. C.; Zin, W.-C.; Chang, T. *Macromolecules* **2008**, *41*, 1760. (k) Park, S.; Ryu, D. Y.; Kim, J. K.; Ree, M.; Chang, T. *Polymer* **2008**, *49*, 2170. (l) Yang, S. Y.; Park, J.; Yoon, J.; Ree, M.; Jang, S. K.; Kim, J. K. *Adv. Funct. Mater.* **2008**, *18*, 1371.

(5) (a) Lee, B.; Park, I.; Yoon, J.; Park, S.; Kim, J.; Kim, K.-W.; Chang, T.; Ree, M. *Macromolecules* **2005**, *38*, 4311. (b) Jin, S.; Yoon,

J.; Heo, K.; Park, H.-W.; Shin, T. J.; Chang, T.; Ree, M. *J. Appl. Crystallogr.* **2007**, *40*, 950. (c) Heo, K.; Yoon, J.; Jin, S.; Kim, J.; Kim, K.-W.; Shin, T. J.; Chung, B.; Chang, T.; Ree, M. *J. Appl. Crystallogr.* **2008**, *41*, 281.

(6) (a) Yoon, J.; Yang, S. Y.; Heo, K.; Lee, B.; Joo, W.; Kim, J. K.; Ree, M. *J. Appl. Crystallogr.* **2007**, *40*, 305. (b) Yoon, J.; Jin, S.; Ahn, B.; Rho, Y.; Hirai, T.; Maeda, R.; Hayakawa, T.; Kim, J.; Kim, K.-W.; Ree, M. *Macromolecules* **2008**, *41*, 8778. (c) Yoon, J.; Jung, S. Y.; Ahn, B.; Heo, K.; Jin, S.; Iyoda, T.; Yoshida, H.; Ree, M. *J. Phys. Chem. B.* **2008**, *112*, 8486.

(7) (a) Manners, I. *Science* **2001**, *294*, 1664. (b) Manners, I. *Angew. Chem., Int. Ed.* **2007**, *46*, 1565.

(8) (a) Ni, Y.; Rulkens, R.; Manners, I. *J. Am. Chem. Soc.* **1996**, *118*, 4102. (b) Massey, J.; Power, K. N.; Manners, I.; Winnik, M. A. *J. Am. Chem. Soc.* **1998**, *120*, 9533. (c) Massey, J. A.; Temple, K.; Cao, L.; Rharbi, Y.; Raez, J.; Winnik, M. A.; Manners, I. *J. Am. Chem. Soc.* **2000**, *122*, 11577.

(9) (a) Lichtenhan, J. D.; Otonari, Y. A.; Carr, M. J. *Macromolecules* **1995**, *28*, 8435. (b) Haddad, T. S.; Lichtenhan, J. D. *Macromolecules* **1996**, *29*, 7302.

(10) (a) Pyun, J.; Matyjaszewski, K. *Macromolecules* **2000**, *33*, 217. (b) Pyun, J.; Matyjaszewski, K.; Wu, J.; Kim, G.-M.; Chun, S. B.; Mather, P. T. *Polymer* **2003**, *44*, 2739. (c) Kim, B.-S.; Mather, P. T. *Macromolecules* **2006**, *39*, 9253. (d) Xu, W.; Chung, C.; Kwon, Y. *Polymer* **2007**, *48*, 6286. (e) Zheng, L.; Farris, R. J.; Coughlin, E. B. *Macromolecules* **2001**, *34*, 8034.

(11) Waddon, A. J.; Zheng, L.; Farris, R. J.; Coughlin, E. B. *Nano Lett.* **2002**, *2*, 1149.

(12) (a) Zheng, L.; Waddon, A. J.; Farris, R. J.; Coughlin, E. B. *Macromolecules* **2002**, *35*, 2375. (b) Waddon, A. J.; Coughlin, E. B. *Chem. Mater.* **2003**, *15*, 4555. (c) Zheng, L.; Hong, S.; Cardoen, G.; Burgaz, E.; Gido, S. P.; Coughlin, E. B. *Macromolecules* **2004**, *37*, 8606.

(13) (a) Ro, H. W.; Kim, K. J.; Theato, P.; Gidley, D. W.; Yoon, D. Y. *Macromolecules* **2005**, *38*, 1031. (b) Zhang, L.; Abbenhuis, H. C. L.; Yang, Q.; Wang, Y.-M.; Magusin, P. C. M. M.; Mezari, B.; van Santen, R. A.; Li, C. *Angew. Chem., Int. Ed.* **2007**, *46*, 5003. (c) Lee, Y.-J.; Huang, J.-M.; Kuo, S.-W.; Lu, J.-S.; Chang, F.-C. *Polymer* **2005**, *46*, 173.

(14) (a) Hayakawa, T.; Seino, M.; Goseki, R.; Hirai, T.; Kikuchi, R.; Kakimoto, M.; Tokita, M.; Yokoyama, H.; Horiuchi, S. *Polym. J.* **2006**, *38*, 567. (b) Hirai, T.; Leolukman, M.; Hayakawa, T.; Kakimoto, M.; Gopalan, P. *Macromolecules* **2008**, *41*, 4558. (c) Hirai, T.; Leolukman, M.; Jin, S.; Goseki, R.; Ishida, Y.; Kakimoto, M.-a.; Hayakawa, T.; Ree, M.; Gopalan, P. *Macromolecules* **2009**, *42*, 8835.

(15) (a) Yoon, J.; Kim, K.-W.; Kim, J.; Heo, K.; Jin, K. S.; Jin., S.; Shin, T. J.; Lee, B.; Rho, Y.; Ahn, B.; Ree, M. *Macromol. Res.* **2008**, *16*, 575. (b) Bolze, J.; Kim, J.; Huang, J.-Y.; Rah, S.; Youn, H. S.; Lee, B.; Shin, T. J.; Ree, M. *Macromol. Res.* **2002**, *10*, 2.

(16) (a) Lee, B.; Park, Y.-H.; Hwang, Y.; Oh, W.; Yoon, J.; Ree, M. *Nat. Mater.* **2005**, *4*, 147. (b) Lee, B.; Oh, W.; Hwang, Y.; Park, Y.-H.; Yoon, J.; Jin, K. S.; Heo, K.; Kim, J.; Kim, K.-W.; Ree, M. *Adv. Mater.* **2005**, *17*, 696. (c) Lee, B.; Yoon, J.; Oh, W.; Hwang, Y.; Heo, K.; Jin, K. S.; Kim, J.; Kim, K.-W.; Ree, M. *Macromolecules* **2005**, *39*, 3395. (d) Lee, B.; Oh, W.; Yoon, J.; Hwang, Y.; Kim, J.; Landes, B. G.; Quintana, J. P.; Ree, M. *Macromolecules* **2005**, *38*, 8991.

(17) (a) Heo, K.; Jin, K. S.; Yoon, J.; Jin, S.; Oh, W.; Ree, M. *J. Phys. Chem. B* **2006**, *110*, 15887. (b) Heo, K.; Oh, K. S.; Yoon, J.; Jin, K. S.; Jin, S.; Choi, C. K.; Ree, M. *J. Appl. Crystallogr.* **2007**, *40*, s614. (c) Jin, K. S.; Heo, K.; Oh, W.; Yoon, J.; Lee, B.; Hwang, Y.; Kim, J.-S.; Park, Y.-H.; Chang, T.; Ree, M. *J. Appl. Crystallogr.* **2007**, *40*, s631. (d) Heo, K.; Park, S. G.; Yoon, J.; Jin, K. S.; Jin, S.; Rhee, S. W.; Ree, M. *J. Phys. Chem. C* **2007**, *111*, 10848.

(18) Kim, G.; Yoon, J.; Kim, J.-S.; Kim, H.; Ree, M. *J. Phys. Chem. B* **2008**, *112*, 8868.

(19) (a) Ree, M.; Ko, I. S. *Phys. High Tech.* **2005**, *14*, 2. (b) Ree, M.; Nam, S. H.; Yoon, M.; Kim, B.; Kim, K.-R.; Kang, T.-H.; Kim, J.-Y.; Kim, K.-J.; Shin, T. J.; Lee, H.-S.; Park, S.-J.; Kim, N.; Lee, K.-B.; Ko, I.-S.; Namkung, W. *Synchrotron Radiat. News* **2009**, *22*, 4.

(20) (a) Liu., Y.; Zheng, S. *J. Polym. Sci., Part A: Polym. Chem.* **2005**, *44*, 1168. (b) Wang, Y.-Z.; Tsai, H.-S.; Ji, Z.-Y.; Chen, W.-Y. *J. Mater. Sci.* **2007**, *42*, 7611.

(21) Bolze, J.; Ree, M.; Youn, H. S.; Chu, S.-H.; Char, K. *Langmuir* **2001**, *17*, 6683.

(22) (a) Yoon, J.; Choi, S.; Jin, S.; Jin, K. S.; Heo, K.; Ree, M. *J. Appl. Crystallogr.* **2007**, *40*, s669. (b) Yoon, J.; Jin, K. S.; Kim, H. C.; Kim, G.; Heo, K.; Jin, S.; Kim, J.; Kim, K.-W.; Ree, M. *J. Appl. Crystallogr.* **2007**, *40*, 476. (c) Yoon, J.; Lee, S. W.; Choi, S.; Heo, K.; Jin, K. S.; Jin, S.; Kim, G.; Kim, J.; Kim, K.-W.; Kim, H.; Ree, M. *J. Phys. Chem. B* **2008**, *112*, 5338. (d) Communications with S. Jin at Postech.

(23) Pedersen, J. S. *J. Appl. Crystallogr.* **1994**, *27*, 595.

(24) Lemmich, J.; Mortensen, K.; Ipsen, J. H.; Hønger, T.; Bauer, R.; Mouritsen, O. G. *Phys. Rev. E* **1996**, *53*, 5169.

(25) Ruland, W.; Smarsly, B. *J. Appl. Crystallogr.* **2004**, *37*, 575.

(26) Hosemann, R.; Bagchi, S. N. *Direct analysis of diffraction by matter*; North-Holland: Amsterdam, 1962.